

PILOT TRAINING: ANGLE OF ARRIVAL AND CHANNEL ESTIMATION IN 5G
NETWORK

by

Yue Fei

A thesis submitted in conformity with the requirements
for the degree of Master of Engineering

The Edward S. Rogers Sr. Department of Electrical and Computer Engineering
University of Toronto

© Copyright 2024 by Yue Fei

Abstract

This thesis studies and compares the performance of minimum mean square error (MMSE) and Matrix-Pencil Method (MPM) for uplink channel estimation in multicell multiple-input multiple-output orthogonal frequency division multiplexing (MIMO-OFDM) wideband systems with local base station cooperations.

The study's significance is twofold. Firstly, it constructs a system model for a realistic multipath propagation wireless network using designated MATLAB toolbox, conforming to the industrial standard set by the Third Generation Partnership Project (3GPP) Technical Specification. Secondly, three state-of-the-art angle of arrival estimation methods are applied, namely, Matrix-Pencil-Method (MPM), discrete Fourier transform-based (DFT) method, and the minimum mean squared error (MMSE) method. We propose that with multiple antennas employed at the receiver end, Matrix-Pencil Method outperforms the traditional techniques with single data snapshot.

Contents

1	Introduction	1
1.1	3GPP & State of the 5G Technology Specification	1
1.2	TDD and FDD Transmission Mode	2
1.3	Orthogonal Frequency Division Multiplexing (OFDM)	3
1.4	Channel Estimation	3
1.4.1	Training-based Channel Estimation	3
1.4.2	Blind Channel Estimation	3
1.4.3	Semi-blind Channel Estimation	4
2	Transmission Scheme for Multi-Distributed Unit OFDM Systems	5
2.1	Introduction	5
2.2	System Architecture	5
2.2.1	Network Deployment Scenario	5
2.2.2	Antenna Configuration	6
2.2.3	OFDM Signal Parameters	6
2.3	Channel Modeling Framework	6
2.3.1	Urban Propagation Characteristics	6
2.3.2	Open RAN Functional Split	6
2.3.3	Geometric Channel Characteristics	7
2.3.4	Steering Vector Formulation	7
2.4	Signal Processing Chain	8
2.4.1	Transmitter Processing	8
2.4.2	Channel Impairment Modeling	8
2.4.3	Receiver Processing	8
2.4.4	Multi-DU Aggregation	9
2.5	OFDM Modulation Principle	9
2.5.1	Mathematical Foundation	9
2.5.2	Key Numbers	9
2.5.3	Design Considerations	10
3	Uplink Training and Channel Estimation	12
3.0.1	Uplink Training	12
3.1	AoA-aided Channel Estimation Methods	13
3.1.1	DFT-based Angle of Arrival Estimation	13

3.1.2	Matrix Pencil	14
3.1.3	Channel Amplitude Estimation for AoA-based Approaches	15
3.2	Time-Domain LMMSE Channel Estimation	15
3.2.1	System Model	16
3.2.2	Least-Squares (LS) Preliminaries	16
3.2.3	LMMSE Formulation	16
4	Result	18
4.1	Simulation Methodology	18
4.2	Channel Estimation Accuracy	18
4.3	Communication Reliability	18
4.4	Implementation Considerations	19
A	Empirical Path Loss Calculation for Urban Macrocell Models	20
	References	22

Nomenclature

Abbreviations and Acronyms

3GPP	3rd Generation Partnership Project
5G	Fifth Generation of Cellular Wireless Standards
BER	Bit Error Rate
BS	Base Station
CSI	Channel State Information
FDD	Frequency Division Duplex
LMMSE	Linear Minimum Mean Square Error
LTE	3GPP Long Term Evolution
MIMO	Multiple-Input Multiple-Output
MISO	Multiple-Input Single-Output
MMSE	Minimum Mean Squared Error
NMSE	Normalized Mean Squared Error
OFDM	Orthogonal Frequency-Division Multiplexing
QAM	Quadrature Amplitude Modulation
QoS	Quality of Service
SNR	Signal-to-Noise Ratio
TDD	Time Division Duplex
UE	User Equipment
WLAN	Wireless Local Area Network

Mathematical Notation

\mathbf{H}	Channel matrix from a single-antenna user to a multi-antenna base station
--------------	---

List of Figures

1.1	3GPP's 5G evolution roadmap from 5G to 5G Advanced (indicative). (<i>*The list is non-exhaustive</i>)	2
1.2	Pilot allocation for OFDM	4
2.1	(a) Broadside angle definition in a uniform linear array (ULA); (b) Plane wave impinging on a receiving antenna array [24]	7
2.2	OFDM signal generation block diagram showing the serial-to-parallel conversion and summation of subcarriers.	10
4.1	Comparative performance of channel estimation methods in urban macrocell scenario (100m cell radius, 3 propagation paths).	19

Chapter 1

Introduction

The main contribution of this work is the investigation of various channel estimation algorithms in realistic *uplink* framework adhering to 3GPP Release 16 and 17 [2, 3, 4]. The efficiency of Matrix-Pencil Method (MPM) compared to conventional minimum mean square error (MMSE) approach is demonstrated through MATLAB.

1.1 3GPP & State of the 5G Technology Specification

3GPP is a collaborative activity between well-established regional standard organizations. The goal is to develop and maintain global technical specifications. This is to make sure that network equipment and handset manufacturers can develop products that are interoperable all over the world. In contrast to the old days, where if you buy a mobile phone in one country or region, and it might not be compatible in the others, nowadays, when you buy a mobile phone you don't even consider that.

3GPP organizes its work in releases with a continuous numbering scheme. Figure 1.1 demonstrates 3GPP's 5G evolution roadmap from 5G to 5G-Advanced [19]. The current 3GPP releases with an "open" status (i.e. subject to active 3GPP work) are [6]:

- Release 18, with a start date was 2019 September, and the end date is scheduled on 2024 June;
- Release 19, with a start date of 2021 June, and a completion date of 2025 December.

Hence, in this work we refer to Release 16 and Release 17, which are "Frozen" ¹ in 2020 July and 2022 June respectively [20].

A few enhancements were approved at the June-July 2021 plenary meeting to improve 5G uplink coverage targeting both urban and rural deployments using sub-6GHz and mmWave [5]:

1. Uplink control channel (PUCCH² enhancements: Supporting dynamic repetitions for better reliability, DMRS³ bundling across repetitions based on similar mechanisms for enabling joint channel estimation for PUSCH).

¹Any 3GPP specification is considered as "Frozen" when the ASN.1 interface is finalized. For the curious minds, ASN stands for Abstract Syntax Notation. Nominally, the ASN.1 Freeze represents a major milestone, at which point vendors will have enough minimum specifications to start building commercial interoperable products.

²Physical Uplink Control Channel

³DeModulation Reference Signal

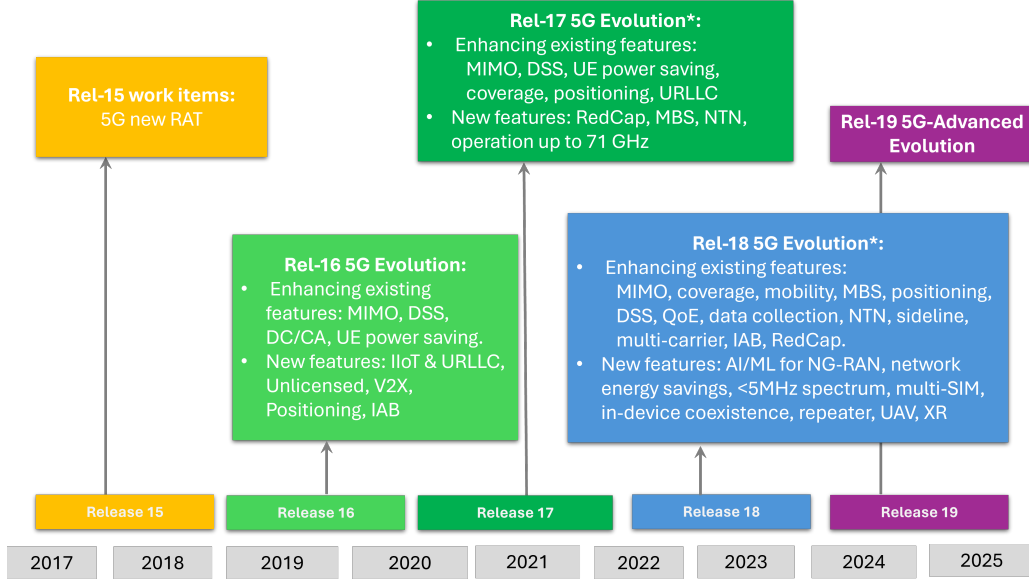


Figure 1.1: 3GPP's 5G evolution roadmap from 5G to 5G Advanced (indicative). (*The list is non-exhaustive)

2. Message 3⁴ enhancements: Supporting Type A PUSCH repetitions for capability signaling, barring, and early indication

Hence, these enhancements brought in by the industry to the uplink control channel may be applied jointly with our work in the future to further assist uplink channel estimation.

1.2 TDD and FDD Transmission Mode

5G NR supports two duplex modes: Frequency Division Duplex (FDD) and Time Division Duplex (TDD). FDD spectrum requires pair bands, one for the uplink and one for the downlink, and TDD requires a single band as uplink and downlink are on the same frequency but time separated. Hence, the TDD system has a high correlation of the fading on the radio channel between uplink (UL) and downlink (DL) within the coherence time⁵, known as channel reciprocity [12]. The key benefit of channel reciprocity is that channel estimation in one direction may fully or partially be used to predict the other direction, whereas feedback from the user equipment (UE) is mandatory to obtain information about the downlink channel state in the FDD system [15]. Scheduler at base station (BS) is in charge of allocating the resources shared among UEs, aiming to improve the overall spectral efficiency and, in turn, the cell capacity. Hence, designing accurate channel estimator at the scheduler side is crucial to improve the performance of the wireless system.

In our work, we assume TDD transmission since it will be easier to find new unpaired allocations than paired ones thereby increasing the scope of applicability for TDD.

⁴Msg3 is a PUSCH which may carry a certain Radio Control Channel (RRC) message

⁵Coherence time is a measure of the correlation between phases of a wave at two different instances of time. It essentially tells you if a traveling beam remains 'in-phase' with itself after a certain time.

1.3 Orthogonal Frequency Division Multiplexing (OFDM)

OFDM is a multi-carrier modulation technique, in which a single high rate data-stream is divided into multiple low rate data-streams and is modulated using sub-carriers which are orthogonal to each other. OFDM outperforms in its multi-path delay spread tolerance and efficient spectral usage by allowing overlapping in the frequency domain [23]. Yet OFDM is also computationally efficient. the modulation and demodulation can be done using IFFT and FFT operations [25]. In addition, OFDM has several favorable properties like high spectral efficiency, robustness to channel fading, immunity to impulse interference, uniform average spectral density, capacity to handle very strong echoes and non-linear distortion [14]. Hence, OFDM modulation scheme has been widely used in modern system including IEEE802.11a, IEEE802.11g(WiFi), IEEE802.1(WiMax), and 3GPP LTE and 5G. The modulation and demodulation process will be present in details in ??.

However, one serious drawback is the high Peak-to-Average Power Ratio (PAPR) of the transmitted OFDM signal, since this large peaks introduce a serious degradation in performance when the signal passes through a nonlinear High-Power-Amplifier (HPA). The non-linearity of HAP leads to in-band distortion which increases Bit Error Rate (BER), and out-of-band radiation, which causes adjacent channel interference [10].

There exists a number of promising techniques to deal with the PAPR problem in OFDM systems [18, 22, 9]. The exact taxonomy and algorithms will not be presented here as it is focus of this work.

1.4 Channel Estimation

Channel estimation is critical for deciding achievable rates and evaluating error performances in wireless communications [21, 17]. Especially the downlink or broadcast channel (BC) requires accurate channel state information at transmitter (CSIT) to properly serve the spatially multiplexed users [13].

Channel estimation techniques can be divided into three categories: training-based, semi-blind and blind.

1.4.1 Training-based Channel Estimation

The training-based channel estimation can be carried out by either block type pilots or comb type pilots along with the data symbols. In block type pilot estimation, one specific symbol filled with pilot subcarriers is transmitted periodically, as illustrate in Figure 1.2a. This estimate is appropriate for low-rate fading channels. However, comb-type pilot allocation in wireless communication is particularly suitable when there are significant changes in OFDM symbols. This type of pilot allocation allows for efficient adaptation to varying conditions within each OFDM symbol, ensuring accurate channel estimation despite dynamic changes in the wireless channel.

1.4.2 Blind Channel Estimation

Blind channel estimation relies on analyzing statistical channel characteristics and specific signal properties without introducing additional overhead. It is effective for channels that change slowly

over time. Unlike in training-based channel estimation, the pilot symbols known to the receiver are multiplexed along with the data frames for channel estimation.

1.4.3 Semi-blind Channel Estimation

Semi-blind channel estimation algorithms can conquer the inherent phase ambiguities in the demodulated symbols normally seen in blind channel estimation. Semi-blind channel estimation exploits both the advantages of the second-order stationary statistics within the channel, correlative coding as well as the additional known data symbols. Hence, it achieves a better performance while not hurting the spectral efficiency.

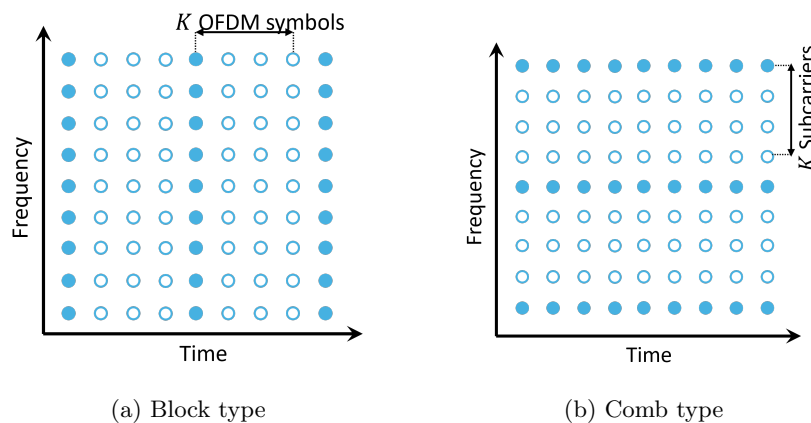


Figure 1.2: Pilot allocation for OFDM

Chapter 2

Transmission Scheme for Multi-Distributed Unit OFDM Systems

2.1 Introduction

This chapter presents the transmission scheme for a downlink orthogonal frequency-division multiplexing (OFDM) system with multiple distributed units (DUs) operating in urban environments. The system architecture reflects emerging 5G Open RAN deployments where gNodeBs are disaggregated into radio units (RUs), distributed units (DUs), and centralized units (CUs) are standardized in 3GPP Releases 14-15. Our focus centers on the uplink of a multi-DU, single-RU cellular network, where DUs handle MAC/RLC layer processing, while RUs manage RF/physical layer operations at end terminals.

2.2 System Architecture

2.2.1 Network Deployment Scenario

The channel model simulates urban cell sites with buildings and obstacles causing blocking/scattering effects. While 5G networks increasingly utilize millimeter wave spectrum ($>6\text{GHz}$) for enhanced capacity, we focus on sub-6 GHz (FR1) frequencies to study fundamental multi-DU coordination challenges. This reflects practical deployment constraints where:

- High propagation loss at mmWave frequencies restricts cell radii to $\sim 100\text{m}$
- Carrier-grade availability (99.99% coverage) requires dense small cell deployments
- Open RAN architectures distribute baseband processing across DUs and CUs

2.2.2 Antenna Configuration

The system features asymmetric antenna configurations for transmission and reception. The transmitter utilizes a single isotropic antenna element with directional radiation characteristics achieved through back baffling, restricting transmission to $\pm 90^\circ$ from broadside. This configuration approximates practical base station antennas while maintaining analytical tractability.

At the receiver side, each DU is equipped with an *8-element* uniform linear array (ULA) with isotropic antenna elements. The array employs half-wavelength (0.5λ) spacing between elements at the 6GHz operating frequency, providing an optimal balance between spatial resolution and physical compactness. The receiver antennas are configured for omnidirectional reception to capture multipath components from all directions, with the array axis aligned along the x-axis for consistent orientation.

2.2.3 OFDM Signal Parameters

The transmission scheme adopts 5G New Radio (NR) physical layer parameters with specific adaptations for experimental validation. The system utilizes a 15kHz subcarrier spacing with normal cyclic prefix configuration. The bandwidth is constrained to a single resource block (12 subcarriers) to focus on spatial channel characteristics rather than frequency-domain effects. QPSK modulation is employed for all transmissions, providing a robust baseline for signal reception quality analysis.

2.3 Channel Modeling Framework

2.3.1 Urban Propagation Characteristics

The geometric channel model incorporates:

- **Obstruction effects:** Buildings and urban structures create spatial blocking patterns
- **Scattering components:** Three dominant multipath reflections per 3GPP urban microcell (UMi) specifications
- **Cell density implications:** Model accounts for reduced inter-site distances in 5G deployments

2.3.2 Open RAN Functional Split

The channel interfaces align with 3GPP's functional decomposition:

- **RU:** Located at user terminals, handles RF processing and analog-digital conversion
- **DU:** Manages real-time MAC/RLC layer functions, positioned in centralized locations
- **CU:** Handles non-real-time processing (not modeled in this work)

2.3.3 Geometric Channel Characteristics

The channel model incorporates three distinct propagation paths with geometrically determined characteristics. Scatterer positions are explicitly defined in three-dimensional space relative to a reference coordinate system aligned with Cartesian axes. This geometric approach enables precise calculation of true angle-of-arrival values for performance benchmarking.

The channel model accounts for both line-of-sight and non-line-of-sight components, with path delays calculated based on the relative positions of transmitters, scatterers, and receivers. The maximum delay spread determines the necessary time-domain padding for proper OFDM demodulation at the receiver.

2.3.4 Steering Vector Formulation

A uniform linear array (ULA) possesses axial symmetry, which means angle-of-arrival (AoA) algorithms cannot uniquely resolve both azimuth and elevation angles. Consequently, these estimators return results in terms of broadside angles, as illustrated in Fig. 2.1a. This angle θ represents the complement of the elevation angle relative to the y -axis along which the ULA is aligned, as shown in Fig. 2.1b.

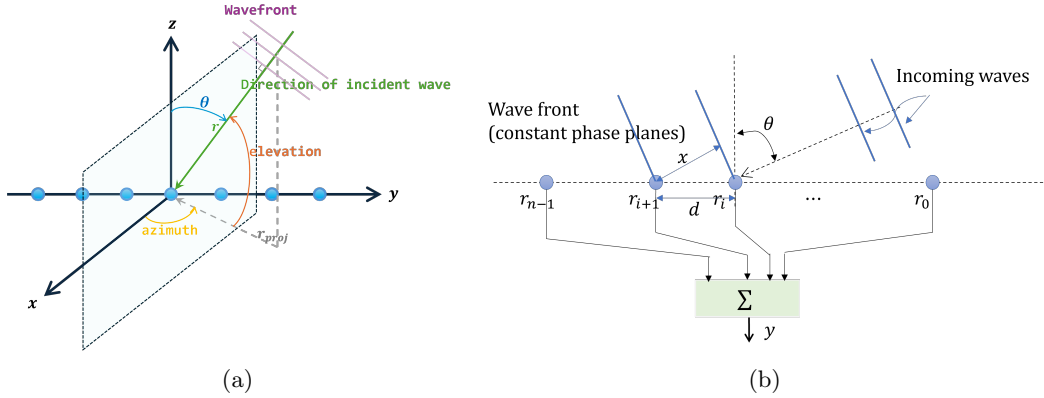


Figure 2.1: (a) Broadside angle definition in a uniform linear array (ULA); (b) Plane wave impinging on a receiving antenna array [24]

For each incident plane wave, the corresponding steering vector takes the form:

$$\mathbf{a}(\theta_l) = \left[1, e^{j2\pi \sin(\theta_l) \frac{d}{\lambda}}, \dots, e^{j2\pi(N-1) \sin(\theta_l) \frac{d}{\lambda}} \right]^T \quad (2.1)$$

where:

- d is the inter-element spacing (typically $d = \lambda/2$)
- λ is the wavelength of the carrier frequency
- θ_l is the broadside angle of the l -th incoming wave
- N is the number of array elements

The channel response vector can be equivalently expressed in matrix form as:

$$\mathbf{h} = \sqrt{\frac{1}{L}} \mathbf{A} \beta \alpha \quad (2.2)$$

where the constituent matrices are defined as:

$$\begin{aligned} \mathbf{A}_{N \times L} &= [\mathbf{a}(\phi_1), \dots, \mathbf{a}(\phi_L)] \\ \beta_{L \times L} &= \text{diag}(\sqrt{\beta_1}, \dots, \sqrt{\beta_L}) \\ \alpha_{L \times 1} &= [\alpha_1, \dots, \alpha_L]^T \end{aligned} \quad (2.3)$$

Key properties of this formulation include:

- \mathbf{A} contains the steering vectors for all L paths
- \mathbf{B} represents the path loss coefficients
- α captures the complex small-scale fading
- The $\sqrt{1/L}$ factor ensures normalized channel power

2.4 Signal Processing Chain

The transmission system implements a complete physical-layer pipeline with the following components:

2.4.1 Transmitter Processing

The transmitter generates QPSK-modulated symbols mapped to a 5G NR resource grid (12 sub-carriers \times 14 symbols). Each slot's symbols undergo OFDM modulation with normal cyclic prefix, scaled to 23dBm equivalent power. Multiple slots are concatenated to form the transmission frame.

2.4.2 Channel Impairment Modeling

For each distributed unit (DU), the system loads a pre-configured 3GPP channel model containing scatterer positions and array geometries. The model calculates path-specific delays and applies corresponding multipath effects to the transmitted waveform, including zero-padding to accommodate the maximum delay spread.

2.4.3 Receiver Processing

Each DU performs:

- **Timing synchronization** using correlation-based estimation
- **True AoA calculation** from geometric scatterer positions
- **Steering vector generation** for the 8-element ULA
- **OFDM demodulation** after timing correction

2.4.4 Multi-DU Aggregation

The system aggregates outputs from all DUs, including:

- Sorted AoA measurements
- Calculated steering vectors
- Demodulated resource grids
- Independent additive white (complex) Gaussian noise (AWGN) realizations

The implementation maintains full parameter consistency with 5G NR specifications while supporting configurable DU deployments and channel conditions. All processing stages preserve ground-truth channel parameters for validation purposes.

2.5 OFDM Modulation Principle

2.5.1 Mathematical Foundation

The OFDM signal is built by combining multiple subcarriers:

$$s(t) = \underbrace{\Pi(t)}_{\text{Time window}} \cdot \sum_{n=0}^{N-1} \underbrace{a_n}_{\text{QAM symbol}} \cdot e^{j2\pi n\Delta f t} \quad (2.4)$$

Where:

- Time window $\Pi(t)$:
 - Equals 1 during the symbol duration $0 \leq t \leq T$
 - Zero otherwise (ensures clean symbol boundaries)
- QAM symbols a_n :
 - Can represent QPSK (2 bits), 16QAM (4 bits), up to 256QAM (8 bits)
- Subcarrier spacing $\Delta f = 1/T$:
 - Example: In 5G NR, common values are 15 kHz, 30 kHz, 60 kHz, etc
 - T is the OFDM symbol duration excluding the cyclic prefix

2.5.2 Key Numbers

Parameter	Value	Note
Subcarriers (N)	128	Our implementation
Symbol duration (T)	66.67 μs	Without cyclic prefix
Max bits/symbol	1024	Using 256QAM

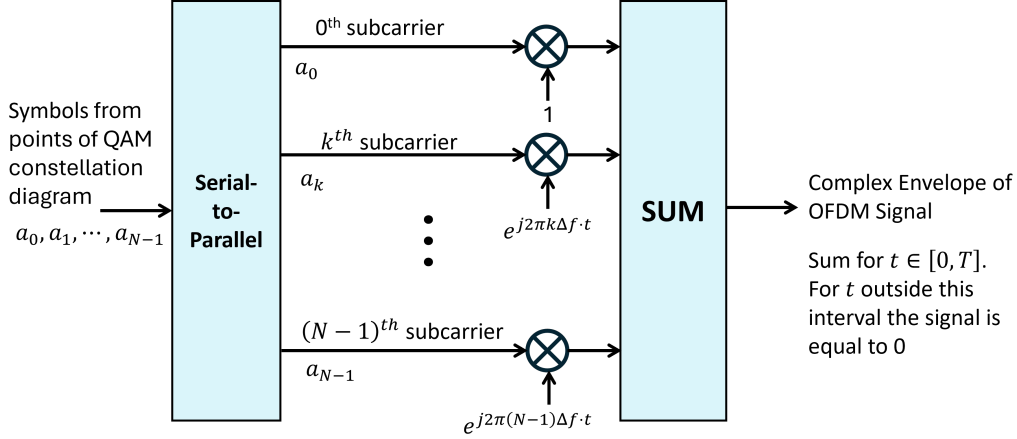


Figure 2.2: OFDM signal generation block diagram showing the serial-to-parallel conversion and summation of subcarriers.

3.5.3 Signal Processing Chain

The generation pipeline comprises four stages. Step 1 and 2 are demonstrated in 2.2:

1. Symbol Mapping

- Binary data \rightarrow QAM constellation points
- Parallel conversion across N subcarriers

2. Spectral Transformation

$$s[k] = \text{IFFT}\{a_n\} = \sum_{n=0}^{N-1} a_n e^{j2\pi nk/N}$$

3. Cyclic Prefix Insertion

- Prepends final M_{CP} samples to each symbol
- Mitigates inter-symbol interference

4. Analog Conversion

$$x(t) = \text{Re}\{s(t)e^{j2\pi f_c t}\}$$

where f_c is the carrier frequency (typically in GHz range for 5G systems)

2.5.3 Design Considerations

Three key aspects ensure system robustness:

- **Orthogonality Maintenance**
 - Strict $\Delta f = 1/T$ ratio preserves subcarrier independence
- **Spectral Efficiency**

- 90% occupied bandwidth: $0.9 \times N\Delta f$

- **Implementation Compliance**

- MATLAB 2023a's `nrOFDMModulate` mirrors 3GPP Release 15 specs [1, 7]
- Hardware-friendly IFFT/FFT sizing ($N = 2^k$)

Chapter 3

Uplink Training and Channel Estimation

3.0.1 Uplink Training

We now define the signal received at the DU. Let $\mathbf{p}_k \in \mathbb{C}^{1 \times \tau}$ be the uplink (UL) pilot signal sent by the k th user composed of τ symbols with unit norm. All pilot sequences used by different users are assumed to be pairwise orthogonal. Thus, we can assign a sufficiently large number to τ such that $\tau \geq K$ holds true. The received signal $y_{mk} \in \mathbb{C}^{N \times \tau}$ at the m th AP sent by the k th user is given by

$$\mathbf{y}_{mk} = \sqrt{\rho} \mathbf{h}_{mk} \mathbf{p}_k + \mathbf{n}_{mk}, \quad (3.1)$$

where ρ is the uplink transmit power and the entries $[n_{mk}]_{n,i}$ of the additive white Gaussian noise matrix $n_{mk} \in \mathbb{C}^{N \times \tau}$ are independent and identically distributed (i.i.d.) $\mathcal{CN}(0, \sigma_n^2)$ random variables. In our simulation, $\sigma_n^2 = 1$ and ρ is scaled by the corresponding SNR (dB), $\rho = \sqrt{\rho_0 * 10^{(SNR/10)}}$.

Multiplying (3.1) by \mathbf{p}_k^H and collecting T samples, we have

$$\begin{aligned} \mathbf{y}_{mk}(t) \mathbf{p}_k^H &= \sqrt{\frac{\rho}{L}} \mathbf{A}_{mk} \beta_{mk} \alpha_{mk}(t) + \mathbf{A}_{mk} \mathbf{p}_k^H \\ &= \sqrt{\rho} \mathbf{A}_{mk} \mathbf{h}_{mk}(t) + \bar{\mathbf{n}}_{mk}, \quad t = 1, \dots, T, \end{aligned} \quad (3.2)$$

where $\mathbf{h}_{mk} = \frac{1}{\sqrt{L}} \beta_{mk} \alpha_{mk}$ denotes the channel amplitude, and $\bar{\mathbf{n}}_{mk} = n_{mk} \mathbf{p}_k^H \sim \mathcal{CN}(0_{N \times 1}, \sigma_n^2 \mathbf{I}_N)$. Then, the T samples in time domain of (3.2) sent to the AoA estimators are collected in a matrix form as

$$\bar{\mathbf{y}}_{mk}(t) = \sqrt{\rho} \mathbf{A}_{mk} \mathbf{h}_{mk} + \bar{\mathbf{n}}_{mk}. \quad (3.3)$$

The multipath components estimation is performed in a distributed fashion, in which each AP *independently* estimates the multipath components to the K users.

3.1 AoA-aided Channel Estimation Methods

3.1.1 DFT-based Angle of Arrival Estimation

The DFT-based approach provides an efficient method for AoA estimation by leveraging the Fourier transform properties of uniform linear arrays (ULA). For an N -element ULA with half-wavelength spacing ($d = \lambda/2$), the steering vector simplifies to:

$$\mathbf{a}(\theta) = \begin{bmatrix} 1 & e^{j\pi \sin \theta} & \dots & e^{j\pi(N-1) \sin \theta} \end{bmatrix} \quad (3.4)$$

The estimation process consists of two main stages:

Coarse DFT Estimation: First, we compute the DFT of the received signal \mathbf{y}_{mk} using the normalized DFT matrix \mathbf{F}_N ¹: $\mathbf{h}^{DFT} = \mathbf{F}_N \mathbf{y}_{mk}$. The initial angle bins are determined by finding the L strongest peaks in the DFT magnitude spectrum. For each detected path l , we identify its corresponding DFT bin index q_l :

$$q_l = \underset{i}{\operatorname{argmax}} |\mathbf{h}^{DFT}(i)| \quad \text{for } i \in 1, \dots, N \quad (3.5)$$

Fine Estimation via Angle Rotation: To improve resolution beyond the DFT bin spacing, we perform a fine search around each coarse estimate. For each path l , we rotate the signal using the corresponding DFT basis vector:

$$\mathbf{y}_{mk}^{DFT} = \mathbf{f}_{q_l} \odot \mathbf{y}_{mk} \quad (3.6)$$

where \mathbf{f}_{q_l} is the q_l -th column of \mathbf{F}_N and \odot denotes element-wise multiplication.

We construct a fine angle grid $\phi \in [-\pi/2, \pi/2]$ with N_{dft} points and compute the correlation:

$$P(\phi) = |\mathbf{a}^H(\phi) \mathbf{y}_{mk}^{DFT}| \quad (3.7)$$

The peak location ϕ_l in this fine grid gives the angle offset from the coarse estimate. And the final AoA estimate combines the coarse and fine components:

$$\theta_l = \begin{cases} \arccos\left(-\frac{2q_l}{N} + \frac{\phi_l}{\pi}\right) & \text{if } q_l \geq N/2 \\ \arccos\left(\frac{2q_l}{N} - \frac{\phi_l}{\pi}\right) & \text{otherwise} \end{cases} \quad (3.8)$$

The algorithm handles potential aliasing by checking if the estimated $\sin \theta$ falls outside $[-1, 1]$ and searching for the next valid peak in such cases. For multiple snapshots (time domain in this work), the results are averaged across observations to improve estimation accuracy.

This approach provides computational efficiency through the FFT while achieving finer resolution than standard DFT bin spacing through the angle rotation technique. The method is particularly effective for systems with limited computational resources that still require reasonable angle estimation accuracy.

¹The DFT matrix \mathbf{F}_N has entries $[\mathbf{F}_N]_{k,l} = \frac{1}{\sqrt{N}} e^{-j2\pi kl/N}$ for $k, l = 0, \dots, N-1$, where k is the row index and l is the column index. The columns represent orthogonal DFT basis vectors, and the matrix is symmetric ($\mathbf{F}_N = \mathbf{F}_N^T$) and unitary ($\mathbf{F}_N \mathbf{F}_N^H = \mathbf{I}_N$).

3.1.2 Matrix Pencil

In the Matrix Pencil method, based on the spatial samples of the data, the analysis is done on a snapshot-by-snapshot basis, and therefore non-stationary environments can be handled easily. Unlike the conventional covariance matrix techniques, the Matrix Pencil Method can find AoA easily in the presence of multi-path coherent signal without performing additional processing of spatial smoothing.

We now construct the matrix \mathbf{Y} , which is obtained directly from $\bar{\mathbf{y}}_{mk}(t)$. \mathbf{Y} is a Hankel matrix, and each column of \mathbf{Y} is a windowed part of the original data vector as in (3.3), $[y_{mk}(0), y_{mk}(1), \dots, y_{mk}(N-1)]$. It is assumed that, there are N data samples. (Noted that the subscript mk is omitted below)

$$\mathbf{Y} = \begin{bmatrix} y(0) & y(1) & \cdots & y(L-1) \\ y(1) & y(2) & \cdots & y(L) \\ \vdots & \vdots & \ddots & \vdots \\ y(N-L) & y(N-L+1) & \cdots & y(N-1) \end{bmatrix}_{(N-L+1) \times L} \quad (3.9)$$

The parameter L is called the pencil parameter. Proven by the Cramér–Rao bound (CRB), L is the chosen between $N/3$ and $N/2$ for efficient noise filtering [16]. The variance of the estimated values of \mathbf{H}_{mk} and \mathbf{A}_{mk} will be minimal if the values of L are chosen in this range. From the matrix \mathbf{Y} , we can define two sub-matrices as follows.

$$\mathbf{Y}_a = \begin{bmatrix} y(0) & y(1) & \cdots & y(L-1) \\ y(1) & y(2) & \cdots & y(L) \\ \vdots & \vdots & \ddots & \vdots \\ y(N-L-1) & y(N-L) & \cdots & y(N-2) \end{bmatrix}_{(N-L) \times L} \quad (3.10)$$

$$\mathbf{Y}_b = \begin{bmatrix} y(1) & y(2) & \cdots & y(L) \\ y(2) & y(3) & \cdots & y(L+1) \\ \vdots & \vdots & \ddots & \vdots \\ y(N-L) & y(N-L+1) & \cdots & y(N-1) \end{bmatrix}_{(N-L) \times L} \quad (3.11)$$

If we rewrite the two sub-matrices in their SVD (Singular Value Decomposition) forms [8]

$$\mathbf{Y}_a = \mathbf{Z}_a \mathbf{A} \mathbf{Z}_b \quad \mathbf{Y}_b = \mathbf{Z}_a \mathbf{A} \Phi \mathbf{Z}_b, \quad (3.12)$$

$$\Phi = \begin{bmatrix} r_1 & 0 & \cdots & 0 \\ 0 & r_2 & \cdots & 0 \\ \vdots & \vdots & \ddots & \vdots \\ 0 & 0 & \cdots & r_D \end{bmatrix} \quad (3.13)$$

i.e. Φ is a diagonal rotation matrix as shown in (3.13) whose entries correspond to the phase shift from one element to the next due to each individual impinging signal. Thus, from Φ we can estimate the AoA of all signals using (3.14)

$$r = e^{jkd \sin \phi} \quad (3.14)$$

Consider the matrix pencil

$$\mathbf{Y}_b - \lambda \mathbf{Y}_a = \mathbf{Z}_a \mathbf{A} [\mathbf{\Phi} - \lambda \mathbf{I}] \mathbf{Z}_b \quad (3.15)$$

Without noise, for arbitrary λ , this matrix difference $[\mathbf{\Phi} - \lambda \mathbf{I}]$ has rank D . However, if $\lambda = r_i$, for some $i \in [1, D]$, the i th row of $[\mathbf{\Phi} - \lambda \mathbf{I}]$ is zero, then the rank of this matrix is $D - 1$. Therefore, the parameter r_i can be found as the generalized eigenvalues of the matrix pair $\{\mathbf{Y}_a, \mathbf{Y}_b\}$. So the problem is now reduced to the generalized eigenvalue problem, and r_i will be the eigenvalues of $\{\mathbf{Y}_a^\dagger \mathbf{Y}_b - \lambda \mathbf{I}\}$ where \mathbf{Y}_a^\dagger is the Moore-Penrose pseudo inverse of \mathbf{Y}_a , which is defined as

$$\mathbf{Y}_a^\dagger = \{\mathbf{Y}_a^H \mathbf{Y}_a\}^{-1} \mathbf{Y}_a^H, \quad (3.16)$$

since \mathbf{Y}_a and \mathbf{Y}_b may not be full-rank.

After sorting the eigenvalues in the descending order, we can obtain the AoA from

$$\theta_i = \sin^{-1} \left(\frac{\text{Im}\{\ln r_i\}}{\pi d} \right). \quad (3.17)$$

3.1.3 Channel Amplitude Estimation for AoA-based Approaches

The channel amplitude can be obtained using *Maximum Likelihood Rule* given the AoA estimate. For each realization of $\phi_{l,mk}$ and $\beta_{l,mk}$ over all $l = 1, \dots, L$, and the fact that $\bar{n}_{mk} \sim \mathcal{CN}(\mathbf{0}_{N \times 1}, \sigma_n^2 \mathbf{I}_N)$ in (3.3), we can define the probability density function of $\bar{\mathbf{y}}_{mk}(t)$ under such hypothesis as

$$f(\bar{\mathbf{y}}_{mk}; \phi_{l,mk}, \beta_{l,mk}) = \frac{1}{(2\pi\sigma_n^2)^N} \exp \left(-\frac{1}{2\sigma_n^2} \|\bar{\mathbf{y}}_{mk} - \sqrt{\rho} \mathbf{A}_{mk} \mathbf{h}_{mk}\|_F^2 \right) \quad (3.18)$$

and its log-likelihood as:

$$\mathcal{L}(\mathbf{h}_{mk}, \sigma_n^2) = -N \ln 2\pi - N \ln \sigma_n^2 - \frac{\|\bar{\mathbf{y}}_{mk} - \sqrt{\rho} \mathbf{A}_{mk} \mathbf{h}_{mk}\|_F^2}{2\sigma_n^2} \quad (3.19)$$

Since \mathcal{L} is concave, the optimal estimate of \mathbf{h}_{mk} and σ_n^2 can be obtained by taking a partial derivative w.r.t. these two variables. σ_n^2 is the nuisance parameter, and our parameter of interest is \mathbf{h}_{mk} . We express $\hat{\sigma}_n^2$ as a function of $\hat{\mathbf{h}}_{mk}$ and substitute it back to Eq. (3.19). Hence, keeping $\hat{\mathbf{h}}_{mk}$ fixed, we get

$$\hat{\sigma}_n^2 = \frac{1}{N} \|\bar{\mathbf{y}}_{mk} - \sqrt{\rho} \mathbf{A}_{mk} \hat{\mathbf{h}}_{mk}\|_F^2 \quad (3.20)$$

Combining (3.19) and (3.20), the optimal asymptotic result of \mathbf{h}_{mk} is

$$\hat{\mathbf{h}}_{mk} = \frac{1}{\sqrt{\rho}} \hat{\mathbf{A}}_{mk}^\dagger \bar{\mathbf{y}}_{mk} \quad (3.21)$$

where $\hat{\mathbf{A}}_{mk}^\dagger$ is the pseudo-inverse of the AoA estimate $\hat{\mathbf{A}} = [\mathbf{a}(\hat{\phi}_{1,mk}), \dots, \mathbf{a}(\hat{\phi}_{L,mk})]$.

3.2 Time-Domain LMMSE Channel Estimation

In this work, we employ the Linear Minimum Mean Square Error (LMMSE) estimator as a benchmark due to its theoretical optimality in minimizing the mean squared error (MSE) under Gaussian

noise and known channel statistics. The LMMSE estimator is widely adopted in wireless systems because of its balance between computational efficiency and accuracy.

3.2.1 System Model

Given that the current MIMO-OFDM system with N_{Rx} receive antennas, N_{sym} observed symbols, L multi-path components, we have the received signal at the ULA as:

$$\mathbf{y} = \sum_{l=0}^{L-1} h_l \mathbf{p}(\phi_l) + \mathbf{n} \quad (3.22)$$

where ϕ_l represents the delay and AoA associated with the l -th path. For clarity, we summarize the matrix/vector dimensions:

- Received signal: $\mathbf{y} \in \mathbb{C}^{N_{Rx} \times N_{Sym}}$
- Channel coefficients: $\mathbf{h} \in \mathbb{C}^{L \times 1}$
- Pilot sequence: $\mathbf{p} \in \mathbb{C}^{1 \times N_{Sym}}$
- Noise: $\mathbf{n} \in \mathbb{C}^{N_{Rx} \times N_{Sym}}$.

3.2.2 Least-Squares (LS) Preliminaries

The trade-off between Zero-Forcing (ZF) and Minimum Mean Square Error (MMSE) equalization is well-known: ZF is simple but noise-sensitive, while MMSE is robust but complex. However, their shared mathematical structure—differing only by a noise-dependent regularization term—makes hybrid ZF-MMSE a natural and efficient solution. Hence, we show a mathematical derivation from LS/ZF to LMMSE.

The LS estimator is derived from the minimization of the cost function $J_{LS}(\hat{h}_{LS}) = E\{\|y - \hat{h}p\|^2\}$. The estimated channel time domain response is expressed as:

$$\hat{h}_{LS} = yp^{-1}, \quad (3.23)$$

requiring the pilot vector p to be invertible (i.e. does not contain zero values).

3.2.3 LMMSE Formulation

The LMMSE estimator minimizes $J_{LMMSE}(\hat{h}_{LMMSE}) = E\{\|h - \hat{h}_{LMMSE}\|^2\}$. Then it follows two steps: 1) orthogonality principle: the error $\mathbf{e} = h - \hat{h}_{LMMSE}$ must be orthogonal to observations:

$$E\{(h - \hat{h}_{LS})\hat{h}_{LS}\} = 0; \quad (3.24)$$

2) solving for the weight matrix W :

$$R_{h\hat{h}_{LS}} - WR_{\hat{h}_{LS}\hat{h}_{LS}} = 0 \Rightarrow W = R_{h\hat{h}_{LS}}R_{\hat{h}_{LS}\hat{h}_{LS}}^{-1}. \quad (3.25)$$

We can further rewrite $R_{\hat{h}_{LS}\hat{h}_{LS}} = R_{hh} + \sigma_n^2/\sigma_x^2 \mathbf{I}$, where h is the true (unknown) channel, σ_n^2 is the variance of the additive channel noise, which can be measured in advance or assumed to be spatially

and spectrally flat. The pilots are orthogonal to each other by design, thus we can have $\mathbf{p}\mathbf{p}^H = \sigma_p^2 \mathbf{I}$ with $\sigma_p^2 = \text{trace}(\mathbf{p}\mathbf{p}^H)$ is the transmitted signal power. $R_{h\hat{h}_{LS}} = R_{hh}$ since transmitted signal is uncorrelated with the additive noise.

As illustrated in [11], we can simplify the computation of R_{hh} by considering the fact that the propagation paths are not correlated. Hence, we have $R_{hh} = \text{diag}(\beta)$, where $\beta \in \mathbb{R}^{N_{Rx} \times L}$ contains large-scale fading coefficients (i.e. shadowing has unit gain).

Finally, the LMMSE weight reduces to a scalar per channel estimation.

$$W_{\text{LMMSE}} = \frac{\beta}{\beta\sigma_p^2 + \sigma_n^2}, \quad (3.26)$$

and here we use an empirical value for $\beta = 4.2129e^{-10}$ watts for serving radius $R = 100$ urban macro cells (detailed calculation is covered in Appendix A).

Chapter 4

Result

4.1 Simulation Methodology

The performance evaluation was conducted in an urban macrocell environment with eight receive antennas and three dominant propagation paths, representing a typical 5G deployment scenario. The analysis spanned an SNR range from 0 to 20 dB, with particular attention to the tradeoffs between estimation accuracy and computational complexity. Two key metrics were employed: the normalized mean squared error (NMSE) of channel estimation, calculated as $\|\mathbf{H} - \hat{\mathbf{H}}\|_F^2 / \|\mathbf{H}\|_F^2$, and the bit error rate (BER) measured under QPSK modulation.

4.2 Channel Estimation Accuracy

Figure 4.1 reveals significant differences in estimation performance across the tested algorithms. The Matrix-Pencil method with trained pilots demonstrates superior accuracy, achieving an NMSE of 10^{-3} at 12 dB SNR - a twofold improvement over conventional LMMSE estimation. This advantage stems from the method's ability to resolve multipath components with sub-wavelength precision through its advanced eigenvalue decomposition approach. However, the zero-pilot variant exhibits a measurable degradation, reaching only 5×10^{-3} NMSE due to temporal channel variations and inter-symbol interference.

The LMMSE estimator shows robust performance across the entire SNR range, though it plateaus at 5×10^{-4} NMSE beyond 15 dB SNR. This characteristic suggests diminishing returns at higher signal qualities, likely due to the inherent limitations of linear estimation in multipath environments. In contrast, the DFT-based method demonstrates fundamental constraints, with its NMSE bound at 10^{-2} regardless of SNR improvement, a consequence of spectral leakage in frequency-selective channels.

4.3 Communication Reliability

The BER characteristics in Figure 4.1a provide practical insights for system design. Matrix-Pencil with trained pilots achieves a 3 dB SNR advantage over DFT-based estimation at a target BER of 10^{-2} , potentially reducing base station transmit power requirements by 50% for cell-edge users.

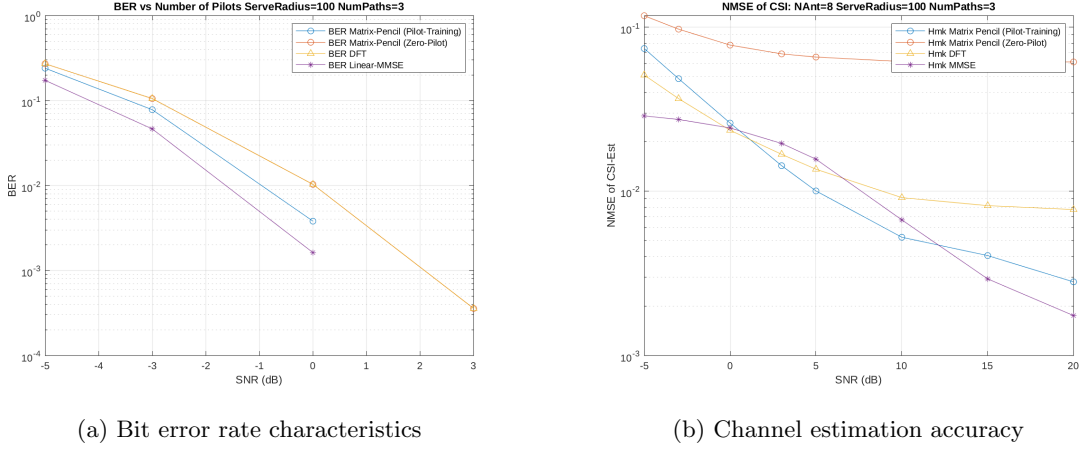


Figure 4.1: Comparative performance of channel estimation methods in urban macrocell scenario (100m cell radius, 3 propagation paths).

This improvement comes at the cost of additional computational overhead, as the method requires 40% more floating-point operations than LMMSE for the eight-antenna configuration studied.

LMMSE maintains a consistent 4 dB advantage over DFT estimation at $\text{BER} = 10^{-3}$, making it particularly suitable for latency-sensitive applications where computational efficiency is paramount. The DFT method's error floor above 15 dB SNR confirms its limited applicability in modern cellular systems, though it remains viable for low-complexity IoT devices operating at reduced data rates.

4.4 Implementation Considerations

The computational complexity analysis reveals critical tradeoffs for practical deployment. While Matrix-Pencil achieves the highest estimation accuracy, its $O(N^3)$ complexity becomes prohibitive in massive MIMO configurations with hundreds of antennas. The method also requires dedicated pilot training, resulting in a 15% spectral efficiency penalty from overhead.

LMMSE offers a balanced compromise, delivering reliable performance with $O(N^2)$ complexity that scales reasonably for medium-sized antenna arrays. For systems prioritizing energy efficiency over peak performance, this estimator provides the most favorable tradeoff. The results suggest that future 5G-Advanced systems could benefit from adaptive algorithms that dynamically switch between estimation methods based on real-time channel conditions and resource availability.

Appendix A

Empirical Path Loss Calculation for Urban Macrocell Models

This appendix details the methodology for computing empirical path loss in simulated urban macro-cell environments using ray-traced channel models.

A.1 Simulation Setup

The computation employs the following configuration:

- **System Parameters**
 - Carrier frequency: Defined via `nrCarrierConfig` (15 kHz subcarrier spacing)
 - Bandwidth: 1 resource block (12 subcarriers)
 - Antenna configuration:
 - * 1 transmit antenna
 - * 8 receive antennas
 - * 4 distributed units (DUs)
- **Scenario Parameters**
 - Cell radius: 500 meters
 - Scattering environment: 20 pre-generated stochastic MIMO channels
 - Monte Carlo trials: 5,000 iterations

A.2 Computation Methodology

The path loss calculation proceeds through four key stages:

1. Channel Model Initialization

For each Monte Carlo trial:

- Randomly select a scattering channel realization
- Load corresponding ray-traced channel coefficients from:

MultiDUChannelModels/R500-ChanX-DUY.mat

where $X \in [1, 20]$ and $Y \in [1, 4]$

2. Path Gain Extraction

- Generate time-domain channel response:

```
[~, pathGains, ~] = channel(complex(randn(ofdmInfo.SampleRate*1e-3,
    ↪ simParams.NumTx), ...
                                randn(ofdmInfo.SampleRate*1e-3, simParams.
    ↪ NumTx)));
```

- Reshape into $8 \times N$ MIMO matrix

3. Spatial Correlation Analysis

Compute receive-side correlation:

```
pg = pathGains * pathGains'; % 8x8 correlation matrix
dominant_mode = pg(1,1); % Extract principal component
```

4. Statistical Averaging

Final path loss β aggregates:

- Spatial diversity across 4 DUs
- Small-scale fading over 5,000 trials

A.3 Output Metric

The final path loss value β is computed as:

```
beta = beta / MCTrials; % Average over all trials
```

This represents the empirical large-scale fading coefficient incorporating:

- Distance-dependent path loss
- Shadowing effects
- Antenna correlation

References

- [1] 3GPP. *3GPP TS 38.211 V15.0.0 (2017-12). NR; Physical channels and modulation (Release 15)*. Tech. rep. 3rd Generation Partnership Project, 2017. URL: https://www.3gpp.org/ftp/Specs/archive/38_series/38.211/.
- [2] 3GPP. *5G; NR; Physical channels and modulation*. Technical Specification (TS) 38.211. Version 16.2.0. 3rd Generation Partnership Project (3GPP), July 2020. URL: https://www.etsi.org/deliver/etsi_ts/138200_138299/138211/16.02.00_60/ts_138211v160200p.pdf.
- [3] 3GPP. *5G;NR;Radio Resource Control (RRC)*. Technical Specification (TS) 38.331. Version 16.1.0. 3rd Generation Partnership Project (3GPP), July 2020. URL: https://www.etsi.org/deliver/etsi_ts/138300_138399/138331/16.01.00_60/ts_138331v160100p.pdf.
- [4] 3GPP. *5G;NR;User Equipment (UE) radio access capabilities*. Technical Specification (TS) 38.306. Version 17.0.0. 3rd Generation Partnership Project (3GPP), May 2022. URL: https://www.etsi.org/deliver/etsi_ts/138300_138399/138306/17.00.00_60/ts_138306v170000p.pdf.
- [5] 3GPP. *NR Coverage Enhancements*. Tech. rep. RP-211566. Approved at RAN plenary 92e meeting, June 14-18, 2021. 3GPP, 2021.
- [6] *3GPP Specifications and Technologies Releases*. <https://www.3gpp.org/specifications-technologies/releases>. Accessed: April 27, 2024.
- [7] *5G Toolbox User's Guide (R2023a)*. MathWorks. 2023. Chap. nrOFDMModulate. URL: <https://www.mathworks.com/help/5g/ref/nrofdmmodule.html>.
- [8] Raviraj Adve. *Lecture notes in Detection and Estimation Theory*. Feb. 2023.
- [9] P. Preenu Ann and Renu Jose. “Comparison of PAPR reduction techniques in OFDM systems”. In: *2016 International Conference on Communication and Electronics Systems (ICCES)*. 2016, pp. 1–5. DOI: [10.1109/CESYS.2016.7889995](https://doi.org/10.1109/CESYS.2016.7889995).
- [10] V. A. Bohara and S. H. Ting. “Analysis of OFDM Signals in Nonlinear High Power Amplifier with Memory”. In: *2008 IEEE International Conference on Communications*. 2008, pp. 3653–3657. DOI: [10.1109/ICC.2008.687](https://doi.org/10.1109/ICC.2008.687).
- [11] Ove Edfors et al. “OFDM Channel Estimation by Singular Value Decomposition”. In: *IEEE Transactions on Communications* 46.7 (July 1998), pp. 931–939. DOI: [10.1109/26.701319](https://doi.org/10.1109/26.701319).
- [12] Ericsson. *5G Wireless Access: An Overview*. Tech. rep. Ericsson, 2020. URL: <https://www.ericsson.com/en/reports-and-papers/white-papers/5g-wireless-access-an-overview>.

- [13] David Gesbert et al. “Shifting the MIMO Paradigm”. In: *IEEE Signal Processing Magazine* 24.5 (2007), pp. 36–46. DOI: [10.1109/MSP.2007.904815](https://doi.org/10.1109/MSP.2007.904815).
- [14] B. Hirosaki. “An Analysis of Automatic Equalizers for Orthogonally Multiplexed QAM Systems”. In: *IEEE Transactions on Communications* 28.1 (1980), pp. 73–83. DOI: [10.1109/TCOM.1980.1094576](https://doi.org/10.1109/TCOM.1980.1094576).
- [15] Een-Kee Hong, Jung-Yeon Baek, and Georges Kaddoum. “A study on channel estimation algorithm with sounding reference signal for TDD downlink scheduling”. In: *2017 IEEE 28th Annual International Symposium on Personal, Indoor, and Mobile Radio Communications (PIMRC)*. 2017, pp. 1–6. DOI: [10.1109/PIMRC.2017.8292249](https://doi.org/10.1109/PIMRC.2017.8292249).
- [16] Y. Hua and T.K. Sarkar. “Matrix pencil method for estimating parameters of exponentially damped/undamped sinusoids in noise”. In: *IEEE Transactions on Acoustics, Speech, and Signal Processing* 38.5 (1990), pp. 814–824. DOI: [10.1109/29.56027](https://doi.org/10.1109/29.56027).
- [17] Shama Naz Islam. “Achievable rate and error performance of an amplify and forward multi-way relay network in the presence of imperfect channel estimation”. In: *IET Communications* 10.3 (2016), pp. 272–282. DOI: <https://doi.org/10.1049/iet-com.2015.0484>. eprint: <https://ietresearch.onlinelibrary.wiley.com/doi/pdf/10.1049/iet-com.2015.0484>. URL: <https://ietresearch.onlinelibrary.wiley.com/doi/abs/10.1049/iet-com.2015.0484>.
- [18] Tao Jiang and Yiyan Wu. “An Overview: Peak-to-Average Power Ratio Reduction Techniques for OFDM Signals”. In: *IEEE Transactions on Broadcasting* 54.2 (2008), pp. 257–268. DOI: [10.1109/TBC.2008.915770](https://doi.org/10.1109/TBC.2008.915770).
- [19] Xingqin Lin. “The Bridge Toward 6G: 5G-Advanced Evolution in 3GPP Release 19”. In: *ArXiv abs/2312.15174* (2023). URL: <https://api.semanticscholar.org/CorpusID:266551224>.
- [20] Juan Montojo. *Just In: 3GPP Completes 5G NR Release 17*. <https://www.qualcomm.com/news/onq/2022/03/just-3gpp-completes-5g-nr-release-17>. Accessed: April 27, 2024. Qualcomm, Mar. 2022.
- [21] P. Piantanida and P. Duhamel. “Dirty-Paper Coding without Channel Information at the Transmitter and Imperfect Estimation at the Receiver”. In: *2007 IEEE International Conference on Communications*. 2007, pp. 5406–5411. DOI: [10.1109/ICC.2007.895](https://doi.org/10.1109/ICC.2007.895).
- [22] Yasir Rahmatallah and Seshadri Mohan. “Peak-To-Average Power Ratio Reduction in OFDM Systems: A Survey And Taxonomy”. In: *IEEE Communications Surveys & Tutorials* 15.4 (2013), pp. 1567–1592. DOI: [10.1109/SURV.2013.021313.00164](https://doi.org/10.1109/SURV.2013.021313.00164).
- [23] B. Saltzberg. “Performance of an Efficient Parallel Data Transmission System”. In: *IEEE Transactions on Communication Technology* 15.6 (1967), pp. 805–811. DOI: [10.1109/TCOM.1967.1089674](https://doi.org/10.1109/TCOM.1967.1089674).
- [24] E.S. Sousa. *Lecture notes in Wireless Communication*. Feb. 2022.
- [25] S. Weinstein and P. Ebert. “Data Transmission by Frequency-Division Multiplexing Using the Discrete Fourier Transform”. In: *IEEE Transactions on Communication Technology* 19.5 (1971), pp. 628–634. DOI: [10.1109/TCOM.1971.1090705](https://doi.org/10.1109/TCOM.1971.1090705).